blood®
Plenary Paper

HEMATOPOIESIS AND STEM CELLS

Bone marrow failure, somatic rescue by p53 inactivation, and enhanced leukemogenesis in germ line ERCC6L2 disease

Roman R. Schimmer,[1] Nancy Klemm,[1] Jonas Fullin,[1] Ebru Topçu,[1] Milena Treacy,[1] Karolina A. Zielińska,[1] Cyril Doerdelmann,[2] Daphne Devesa-Serrano,[2] Melissa Lock,[1] Francisco Caiado,[1] Christian Koch,[1] Nadja Dietliker,[1] Rahel Schwotzer,[1] Marco Bühler,[3,4] Mikko Myllymäki,[5,6] Kari J. Kurppa,[7,8] Markus G. Manz,[1,3] Massimo Lopes,[2] and Steffen Boettcher[1,3]

[1]Department of Medical Oncology and Hematology, University of Zurich and University Hospital Zurich, Zurich, Switzerland; [2]Institute of Molecular Cancer Research, University of Zurich, Zurich, Switzerland; [3]Comprehensive Cancer Center Zurich, Zurich, Switzerland; [4]Department of Pathology and Molecular Pathology, University Hospital Zurich, Zurich, Switzerland; [5]Hematology Research Unit Helsinki, University of Helsinki and Helsinki University Hospital Comprehensive Cancer Center, Helsinki, Finland; [6]Translational Immunology Research Program and Department of Clinical Chemistry and Hematology, University of Helsinki, Helsinki, Finland; [7]Institute of Biomedicine and MediCity Research Laboratory, University of Turku, Turku, Finland; and [8]Turku Bioscience Centre, University of Turku and Åbo Akademi University, Turku, Finland

KEY POINTS

- **Ercc6l2 deficiency leads to replication stress, p53 pathway activation, and decreased *Runx1* and *Gata1* expression resulting in BMF.**
- **Somatic *Trp53* mutations increase the fitness of Ercc6l2-deficient HSPCs, thereby rescuing the BMF at the expense of a leukemogenic risk.**

Recessively inherited loss-of-function mutations in excision repair cross-complementing 6–like 2 (*ERCC6L2*) cause a bone marrow failure (BMF) syndrome characterized by moderate cytopenias, frequent somatic *TP53* mutations, and a propensity to develop myeloid malignancies. The pathophysiology and molecular mechanisms underlying the BMF syndrome as well as its association with *TP53*-mutant clonal hematopoiesis and myeloid malignancies have remained poorly understood. Using novel preclinical in vitro and in vivo model systems, we demonstrate that Ercc6l2 maintains the competitive fitness of hematopoietic stem and progenitor cells (HSPCs) by mitigating replication stress. Sustained replication stress and DNA damage in Ercc6l2-deficient HSPCs cause p53 pathway activation followed by cell cycle arrest and apoptosis. Moreover, Ercc6l2 deficiency results in decreased expression of master hematopoietic regulators *Runx1* and *Gata1* in HSPCs. Altogether, loss of Ercc6l2 leads to reduced HSPC numbers, bone marrow hypocellularity, and cytopenias. Notably, somatic *Trp53* mutations restore cellular fitness of Ercc6l2-deficient HSPCs by abrogating p53 pathway activation and restoring *Runx1* and *Gata1* expression, thereby correcting the BMF phenotype. However, p53 loss fails to normalize replication stress, allowing for the accumulation of DNA damage over time, which increases the likelihood for leukemic transformation. Our data uncover the pathogenesis of ERCC6L2 disease and provide a prototypic example of clonal compensation in BMF syndromes, in which somatic mutations in leukemia-associated genes, in this case *TP53*, transiently improve blood cell production at, however, the expense of increasing leukemogenic potential.

Introduction

Germ line biallelic loss-of-function mutations in excision repair cross-complementing 6–like 2 (*ERCC6L2*) have recently been identified to cause an inherited bone marrow failure (BMF) syndrome.[1] Patients develop adolescent-onset BMF characterized by moderate pancytopenia with anemia and thrombocytopenia being the most common cytopenias.[2] Nonhematologic organ manifestations are rare and likely the product of consanguinity rather than gene-linked consequences.[3-5] Interestingly, there is a strong association of ERCC6L2 disease, clonal hematopoiesis (CH) with somatic *TP53* mutations, and the development of myeloid malignancies. Compared with other leukemia-predisposition syndromes, myeloid malignancies developing in patients with ERCC6L2 disease almost uniformly (>90% of cases) harbor biallelic *TP53* mutations with a strong predilection for acute erythroid leukemias (AELs).[6]

Although the clinical syndrome of ERCC6L2 disease has been well described (roughly 100 cases have been published),[1-3,6-8] the underlying molecular mechanisms and pathophysiology of this disease remain poorly understood. In part, this is due to the sparsely characterized functions of ERCC6L2, involving DNA replication, centromere stability, and DNA repair.[5,7-9] Furthermore, lack of appropriate preclinical model systems

has impeded the gain of further molecular insights into the pathogenesis of ERCC6L2 disease. Importantly, it is unclear how ERCC6L2 deficiency causes BMF, why there is such a strong selection for somatic *TP53* mutations, and how this phenomenon contributes to the development of myeloid malignancies, particularly AELs.

In this study, we developed novel preclinical in vitro and in vivo model systems that faithfully recapitulate key clinical aspects of ERCC6L2 disease. Moreover, we elucidate its pathogenesis and the role of somatic *TP53* mutations in compensating the BMF phenotype at the expense of a higher risk for leukemic transformation.

Methods

Cell line generation

For the generation of CRISPR-associated protein 9 (Cas9)–Lim homeobox protein 2 (Lhx2) cells, $Lin^{-}Sca\text{-}1^{+}c\text{-}kit^{+}$ (LSK^{+}) cells were sorted from whole bone marrow (WBM) of Rosa26-Cas9-knockin (Rosa26-Cas9-KI) mice[10] and transduced with pL-MSCVneo-ER-Lhx2. Cas9–homeobox protein B8 (Hoxb8) cells were generated by transducing WBM cells of Rosa26-Cas9-KI mice with pL-MSCVneo-ER-Hoxb8.

Gene editing

CRISPR/Cas9-mediated gene editing was performed using cells from the Rosa26-Cas9-KI mice.[10] Guide RNA (gRNA) delivery vectors based on the pL-sgRNA.SFFV.fluorochrome backbone were used. All gRNAs used can be found in supplemental Table 2, available on the *Blood* website. Fluorochrome-positive cells were sorted to generate pure CRISPR-edited cell lines. Gene editing efficiency was confirmed via next-generation sequencing, immunoblotting, as well as quantitative reverse transcription polymerase chain reaction.

Competitive cell growth assays

Cas9-Hoxb8 cells of various genotypes and expressing different fluorochromes were seeded at a 1:1 ratio in 96-well flat-bottom plates and cultured in the presence of dimethyl sulfoxide (DMSO) or experimental conditions for up to 16 days. Every 2 days, relative composition of cells was determined by fluorescence-activated cell sorting.

Transformation assay

Cas9-Hoxb8 cells were repetitively treated with either DMSO, high-dose etoposide, or cisplatin for 1 hour followed by recovery periods. Subsequently, β-estradiol was gradually removed, and cultures were monitored for the development of β-estradiol–independent cell growth.

Mouse experiments

Noncompetitive as well as competitive bone marrow (BM) transplantation experiments were performed using CRISPR-edited LSK cells from Rosa26-Cas9-KI mice. A total of 50 000 LSK cells were injected into lethally irradiated C57BL/6 recipient mice, either with or without 0.5×10^{6} $CD45.1^{+}$ WBM cells. Mice were bled every 4 weeks and peripheral blood (PB) counts, chimerism, and CRISPR-editing efficiency were measured. Some mice were subjected to 2 sublethal irradiations spaced 4 weeks apart starting at 3 months after transplantation and monitored for the development of malignancies. At terminal analysis, the PB, BM, and spleen, and tumors (if applicable) were processed for further analyses (such as histology, flow cytometry, DNA extraction, etc).

Results

Establishing in vitro models of ERCC6L2 disease and concomitant *TP53*-mutant CH

Given the strong clinical association between germ line *ERCC6L2* and somatic *TP53* mutations, we set out to develop novel preclinical models to study ERCC6L2 disease and the role of concomitant *TP53*-mutant CH. Pooling data from published studies[1-3,5-8] confirmed that >90% of germ line *ERCC6L2* (*E6L2*) mutations in patients are frame-shift and/or nonsense loss-of-function (Figure 1A). Furthermore, irrespective of the specific *ERCC6L2* mutation, affected patients show similar tendencies to develop acute myeloid leukemia (AML).[2] Moreover, human and murine E6L2 show almost 100% protein homology (Figure 1B). Notably, somatic *TP53* mutations in ERCC6L2 disease (Figure 1C) mirror the mutational spectrum found in patients with myeloid malignancies that are known to be loss-of-function mutations.[11] Therefore, we considered CRISPR/Cas9-mediated knock out (CRISPR-KO) of *E6l2* and/or *Trp53* in murine cells a suitable approach for modeling ERCC6L2 disease and *TP53*-mutant CH in vitro.

To this end, we used overexpression of the Lhx2 in mouse BM cells to establish an immortalized hematopoietic stem and progenitor (HSPC) cell line (termed Lhx2 cells) containing a stable multipotent progenitor 2 fraction[12] (supplemental Figure 1A). We modified this model for reversible immortalization by estrogen-dependent Lxh2 expression. Accordingly, upon estrogen withdrawal, Lhx2 cells terminally differentiate into mature blood cells depending on cytokine supplementation (supplemental Figure 1B-C). Lhx2 cells were derived from Rosa26-Cas9-KI mice[10] to facilitate CRISPR/Cas9-mediated gene editing (Figure 1D). We introduced single or combined *E6l2* and/or *Trp53* frame-shift mutations by lentiviral delivery of vectors expressing gRNAs and fluorochromes followed by fluorescence-activated cell sorting for cells with viral integration (Figure 1D). Lhx2 cells transduced with vectors containing nontargeting gRNA served as wild-type controls (nontargeting wild type). Indels were confirmed by CRISPR sequencing, *E6l2* and/or p53 loss by quantitative reverse transcription polymerase chain reaction or western blot, respectively (Figure 1E-F; supplemental Figure 1D). Although we found no cytomorphological differences between Lhx2 cells of all 4 genotypes (ie, nontargeting wild type, *E6l2*-KO, *Trp53*-KO, and *E6l2-Trp53*-KO; supplemental Figure 1E), *E6L2*-KO Lhx2 cells showed severely impaired cell growth, decreasing viabilities over time, increased levels of apoptosis, and reduced LSK percentages (Figure 1G-K), resulting in an almost complete loss of clonogenic potential (Figure 1L; supplemental Figure 1F). Importantly, *Trp53* mutations fully reversed these defects observed upon E6l2 loss (Figure 1G-L; supplemental Figure 1F). Although these results demonstrate that loss of E6l2 in Lhx2 cells causes a severe HSPC defect in vitro

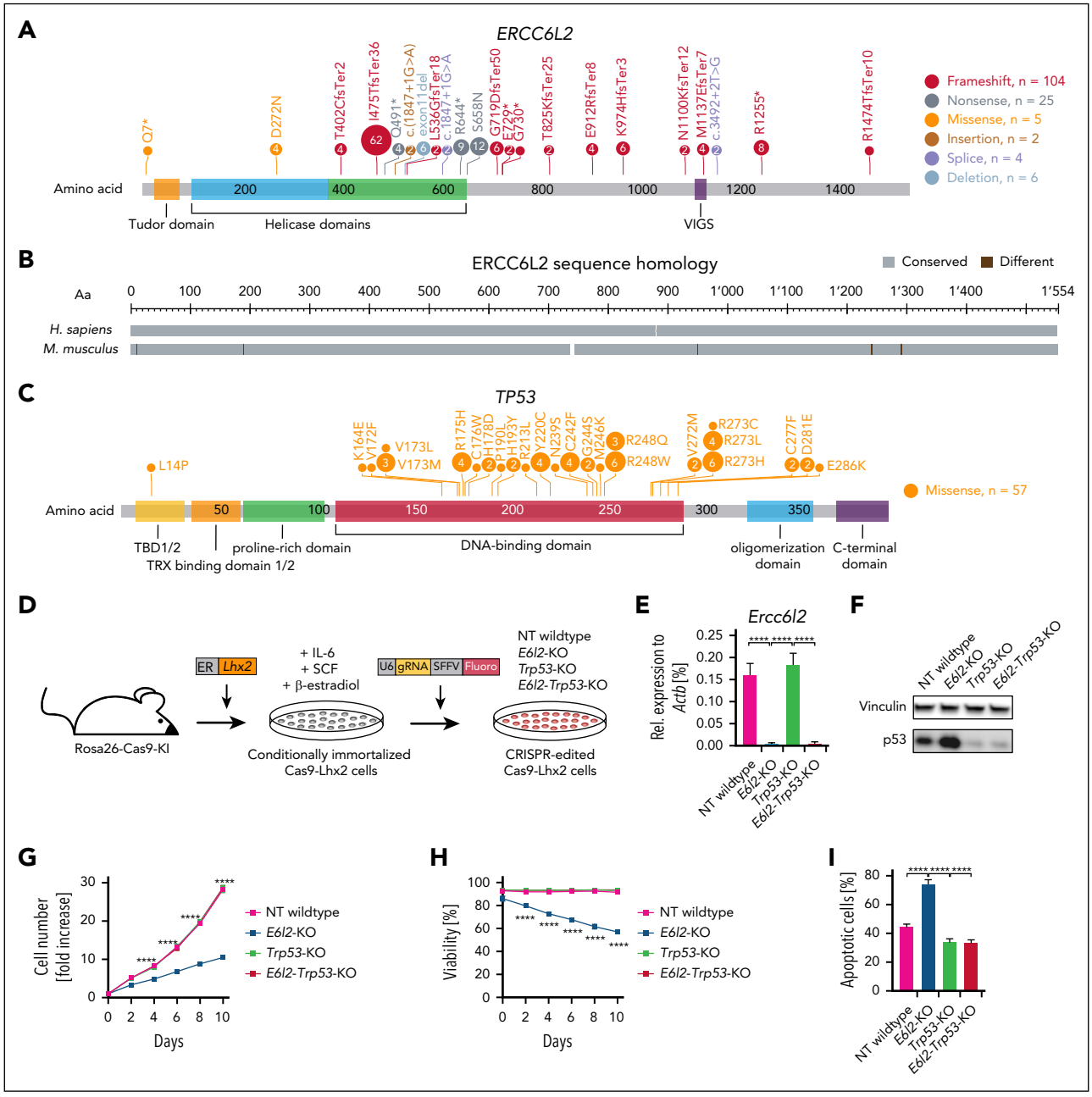

Figure 1. Novel preclinical in vitro and in vivo models to study ERCC6L2 disease. (A) Lollipop plot demonstrating germ line *ERCC6L2* mutational spectrum from all published cases of ERCC6L2 disease.[1-3,5-8] Protein domains: orange, Tudor domain; blue and green, helicase domains; purple, VIGS (highly conserved region of unknown function). (B) Graphical representation of amino acid sequence homology between human ERCC6L2 and mouse Ercc6l2. Amino acid differences are highlighted in purple. Data extracted from the National Center for Biotechnology Information. (C) Lollipop plot depicting somatic *TP53* mutational spectrum from all published patients with ERCC6L2 disease who developed *TP53*-mutant myeloid malignancies.[2] Protein domains: yellow, TBD1/2; orange, TRX-binding domain 1/2; green, proline-rich domain; red, DNA-binding domain; blue, oligomerization domain; purple, C-terminal domain. (D) Experimental schematic for the generation of conditionally immortalized Cas9-Lhx2 cells and subsequent CRISPR editing. (E) quantitative reverse transcription polymerase chain reaction (RT-qPCR) measuring expression of *Ercc6l2* transcripts normalized to *Actb* in CRISPR-engineered Cas9-Lhx2 cells (n = 3 independent experiments, bar graphs represent averages, error bars indicate standard error of the mean [SEM], $^{****}P \leq .0001$, Student *t* test). (F) Whole-cell lysates of CRISPR-edited Cas9-Lhx2 cell lines of the indicated genotypes at baseline were separated on a polyacrylamide gel and immunoblotted for p53 and vinculin (representative blot of n = 3 independent experiments). (G) Proliferation kinetics of Cas9-Lhx2 cells of indicated genotypes shown as fold increase relative to day 0 (n = 4 independent experiments, symbols represent averages, error bars indicate SEM, $^{****}P \leq .0001$, 2-way analysis of variance [ANOVA], Tukey multiple comparison). (H) Cell viabilities of Cas9-Lhx2 cells of respective genotypes starting directly after cell sorting for positively integrated single guide RNA (sgRNA) vectors (n = 4 independent experiments, symbols represent averages, error bars indicate SEM, $^{****}P \leq .0001$, 2-way ANOVA, Tukey multiple comparison). (I) Percentage of steady-state apoptosis in Cas9-Lhx2 cells as determined by annexin V staining 10 days after fluorescence-activated cell sorting (FACS; n = 4 independent experiments, bar graphs represent averages, error bars indicate SEM, $^{****}P \leq .0001$, 1-way ANOVA, Tukey multiple comparison). (J) Representative FACS plots of LSK ($Lin^{-}Sca\text{-}1^{+}c\text{-}kit^{+}$) populations within Cas9-Lhx2 cells of the indicated genotypes. (K) Percentages of LSKs within CRISPR-edited Cas9-Lhx2 cells (n = 4 independent experiments, bar graphs represent averages, error bars indicate SEM, $^{****}P \leq .0001$, 1-way ANOVA, Tukey multiple comparison). (L) Number of BFU-E colonies. A total of 1.5×10^3 CRISPR-edited LSK Cas9-Lhx2 cells were plated in BFU-E selective methylcellulose-based medium and incubated for 10 days. Analysis was performed using the Colony Area ImageJ plugin followed by manual counting of the colonies (n = 3 independent experiments, bar graphs represent averages, error bars indicate SEM, $^{****}P \leq .0001$, $^{***}P \leq .001$, 1-way ANOVA, Tukey multiple comparison). (M) Experimental schematic for the generation of conditionally immortalized Cas9-Hoxb8 cells and

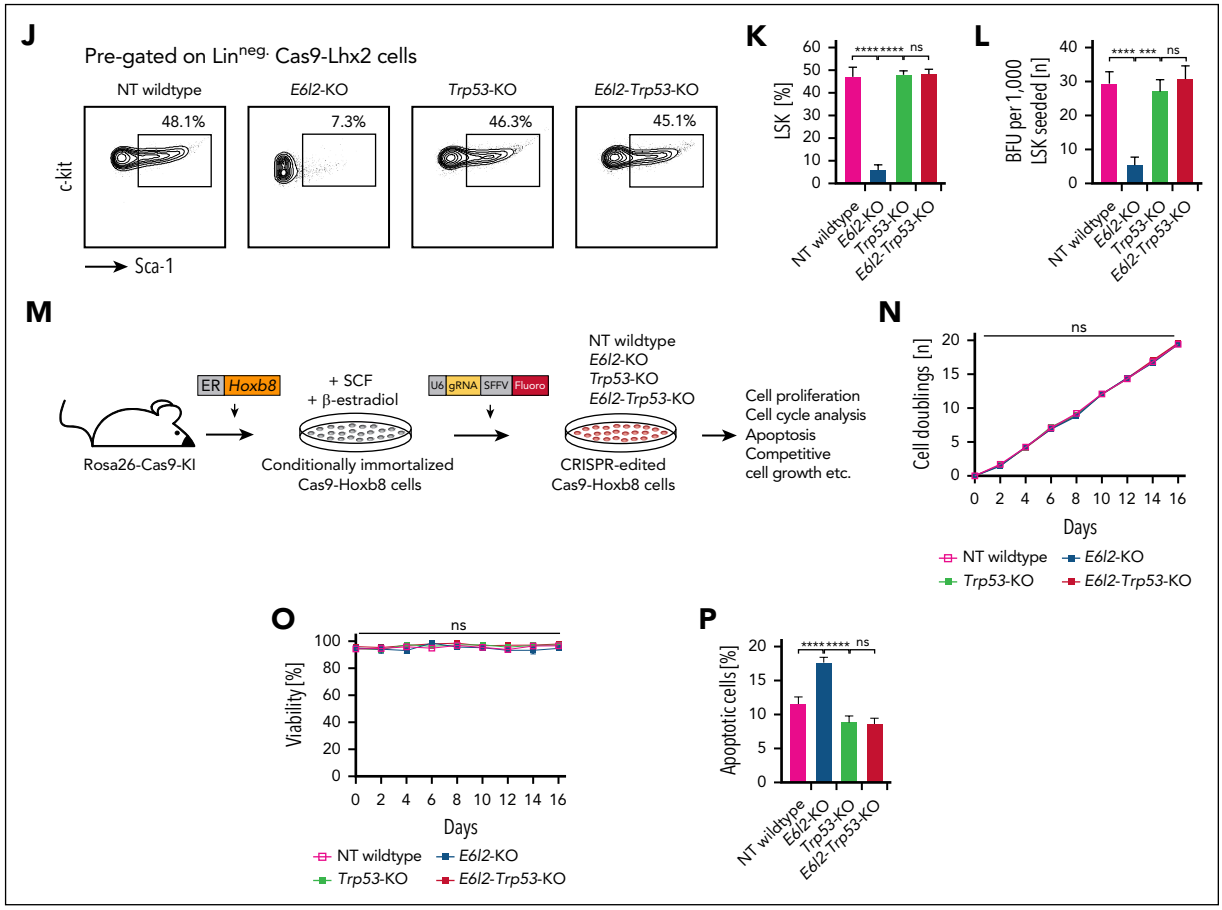

Figure 1 (continued) their subsequent CRISPR editing. (N) Proliferation kinetics of Cas9-Hoxb8 cells of indicated genotypes shown as cell doublings over time (n = 4 independent experiments, symbols represent averages, error bars indicate SEM, 2-way ANOVA, Tukey multiple comparison). (O) Cell viabilities of Cas9-Hoxb8 cells of respective genotypes over time starting directly after cell sorting for positively integrated sgRNA vectors (n = 3 independent experiments, symbols represent averages, error bars indicate SEM, 1-way ANOVA, Tukey multiple comparison). (P) Percentage of steady-state apoptosis in Cas9-Hoxb8 cells as determined by annexin V staining (n = 4 independent experiments, bar graphs represent averages, error bars indicate SEM, $^{****}P \leq .0001$, 1-way ANOVA, Tukey multiple comparison). ER, estrogen receptor; ns, nonsignificant; NT, nontargeting; Rel., relative; SCF, stem-cell factor; VIGS, virus-induced gene silencing.

reminiscent of BMF in patients, its deleterious impact on cell growth and viability of Lhx2 cells precluded further functional and mechanistic studies. We therefore generated another reversibly immortalized mouse HSPC cell line via estrogen-driven Hoxb8 overexpression in BM cells[13] derived from Rosa26-Cas9-KI mice, hereafter termed Hoxb8 cells (Figure 1M). In contrast to Lhx2 cells, Hoxb8 cells are arrested at the more committed granulocyte-monocyte progenitor stage, terminally differentiate into granulocytes and macrophages upon estrogen withdrawal (supplemental Figure 1G) and, importantly, are known to be very robustly proliferating.[13] Accordingly, CRISPR-KO of *E6l2* did not cause relevant baseline differences in proliferation kinetics, viabilities, cell cycle distribution, or differentiation potential in Hoxb8 cells (Figure 1N-O; supplemental Figure 1H-K). As with *E6l2*-KO Lhx2 cells, baseline apoptotic rate in *E6l2*-KO Hoxb8 cells was slightly increased but reversed to levels observed in nontargeting wild-type Hoxb8 cells upon concomitant *Trp53*-KO (Figure 1P). These findings were consistent for 3 different *E6l2*-targeting gRNAs (supplemental Figure 1L-P). Altogether, these data suggest that the inherent robustness of Hoxb8 cells allows stable proliferation despite E6l2 loss and higher baseline apoptosis, thereby enabling further mechanistic studies. Yet, we hypothesized that harsher environmental conditions, likely present in the BM in vivo, might be necessary to reveal the HSPC defect in Hoxb8 cells caused by loss of E6l2.

Ercc6l2 deficiency results in an HSPC defect in vitro and in vivo that is rescued by p53 loss

To unmask the assumed HSPC defect caused by E6l2 deficiency, we treated Hoxb8 cells of all 4 genotypes with both naturally occurring (ie, high cell density, nutrient deficiency, increased reactive oxygen species, or hypoxia) as well as iatrogenic (ie, chemotherapeutic agents etoposide, bleomycin, or cisplatin) stressors (Figure 2A). Indeed, *E6l2*-KO Hoxb8 cells demonstrated p53 pathway activation already at steady-state conditions evidenced by p53 stabilization and enhanced *Cdkn1a*/p21 expression, which were further increased upon stress (Figure 2B-C). This caused G1 arrest and higher apoptosis in *E6l2*-KO cells compared with nontargeting wild-type cells (Figure 2D-E; supplemental Figure 2A-B). Ultimately, this hypersensitivity to cellular stress led to markedly reduced competitive fitness of *E6l2*-KO relative to nontargeting wild-type Hoxb8 cells as determined by in vitro competitive cell growth assays (Figure 2F-G; supplemental

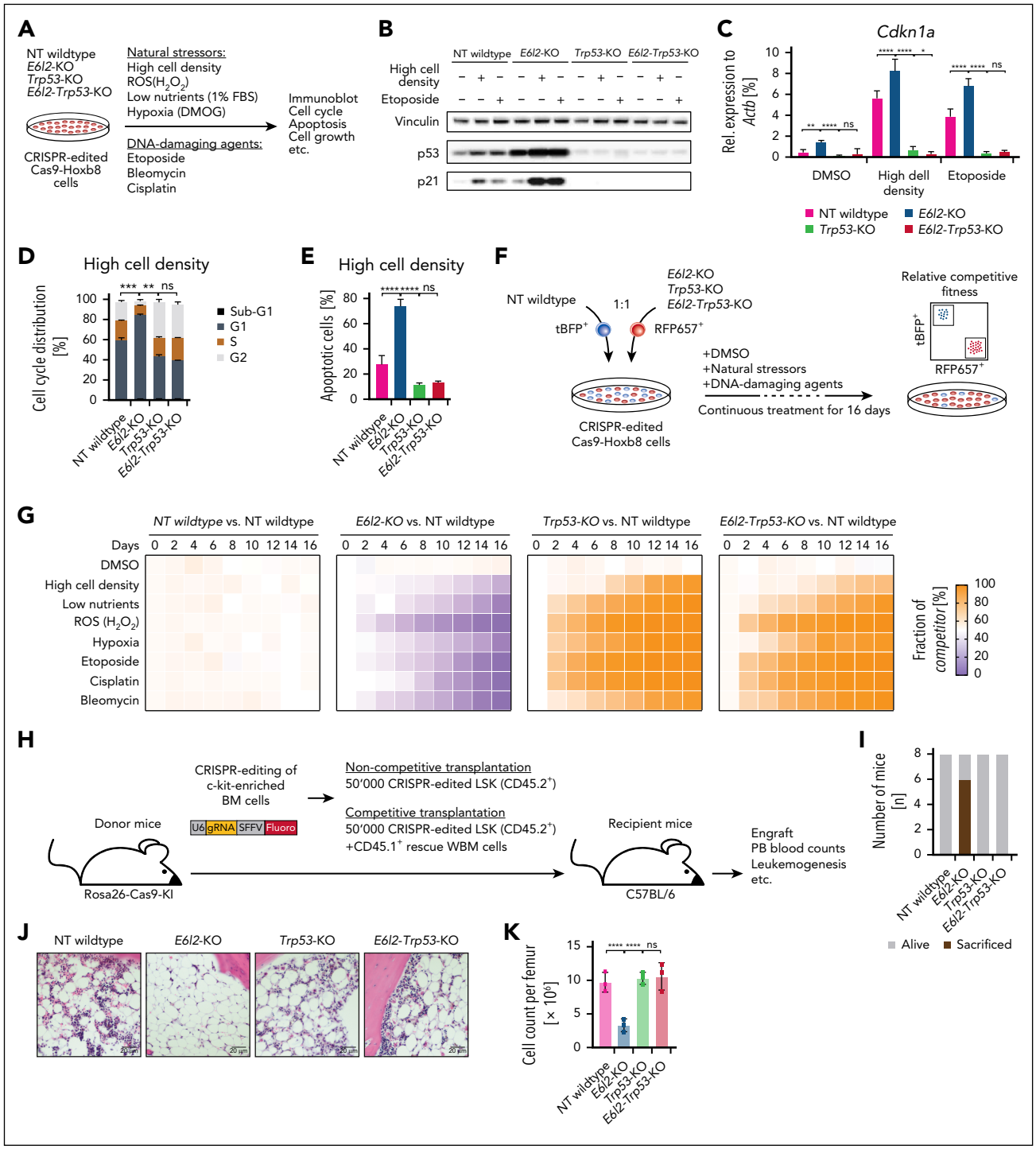

Figure 2. HSPC defect caused by Ercc6l2 deficiency is rescued by p53 loss in vitro and in vivo. (A) Experimental schematic to unmask E6l2-associated HSPC defect in Cas9-Hoxb8 cells. (B) Whole-cell lysates of CRISPR-edited Cas9-Hoxb8 cell lines of the indicated genotypes treated for 3 hours with either DMSO or 10mM etoposide or cultured at high cell density for 48 hours were separated on a polyacrylamide gel and immunoblotted for p53, p21, and vinculin (representative blot of n = 3 independent experiments). (C) RT-qPCR measuring expression of *Cdkn1a* transcripts normalized to *Actb* in Cas9-Hoxb8 cells of indicated genotypes treated either with DMSO or 10mM etoposide for 3 hours or cultured at high cell density for 48 hours (n = 3 independent experiments, bar graphs represent averages, error bars indicate SEM, $^{****}P \leq .0001$, $^{**}P \leq .01$, $^{*}P \leq .05$, 1-way ANOVA, Tukey multiple comparison). (D) Cell cycle distribution of Cas9-Hoxb8 cells of the indicated genotypes after culture at high cell density for 48 hours as determined by DRAQ7 stains (n = 3 independent experiments, bar graphs represent averages, error bars indicate SEM, $^{***}P \leq .001$, $^{**}P \leq .01$, 2-way ANOVA, Tukey multiple comparison). (E) Percentage of apoptotic Cas9-Hoxb8 cells of respective genotypes after culture in high cell density for 48 hours as determined by annexin V staining (n = 3 independent experiments, bar graphs represent averages, error bars indicate SEM, $^{****}P \leq .0001$, 1-way ANOVA, Tukey multiple comparison). (F) Schematic depiction of the experimental principle behind the in vitro competitive cell growth assay. Fluorescently labeled Cas9-Hoxb8 cells of various genotypes were cocultured at a 1:1 ratio in the presence of DMSO and natural, as well as nonnatural, stressors, and the relative percentages of each genotype were determined by flow cytometry every other day for 16 days. (G) Heat maps depicting results of the in vitro competitive cell growth assay described in panel F. Concentrations of drugs used: H_2O_2 at 2.5mM, DMOG (hypoxia-mimetic) at 1mM, etoposide at 150nM, cisplatin at 500nM, bleomycin at 1mM (n = 3-4 independent

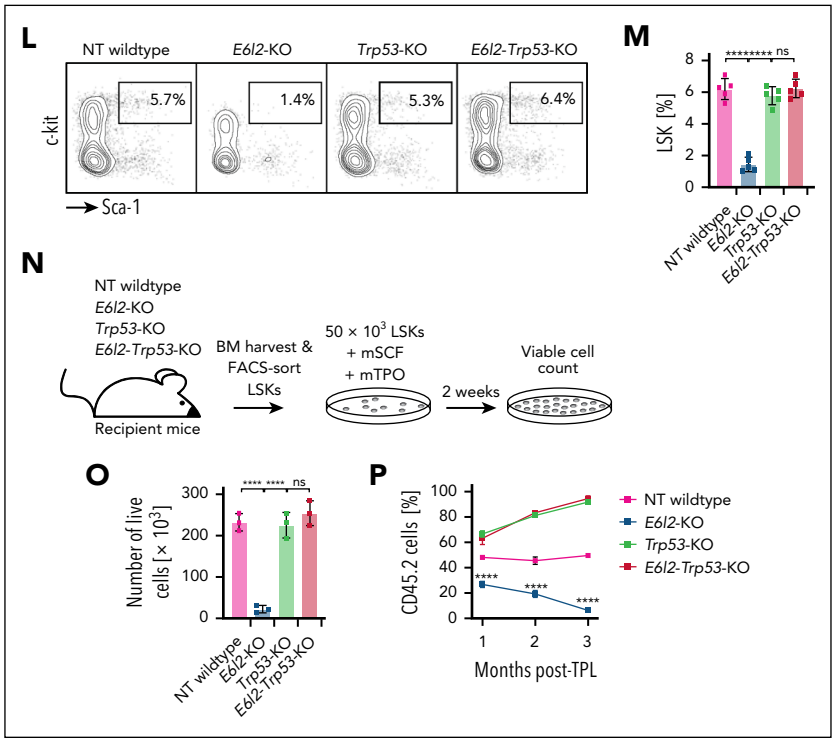

Figure 2 (continued) experiments, color-coded averages are shown). (H) Experimental schematic for in vivo assays. c-kit–enriched BM cells from Rosa26-Cas9-KI mice were transduced with different gRNA-containing vectors, and sorted to obtain LSK cells of all 4 genotypes. A total of 50 000 LSK cells were then injected either alone or with 0.5×10^6 CD45.1 WBM cells into lethally irradiated wild-type recipients. (I) Number of recipient mice alive at 2 months after noncompetitive transplantation with CRISPR-edited LSKs of indicated genotypes (n = 8 animals per group). (J) Representative hematoxylin and eosin (H&E)-stained BM histology taken at 2 months from recipient mice that received noncompetitive transplantation as described in panel H. Scale bars, 20 µm. (K) Cell count per femur from mice of the indicated genotypes taken at 2 months after noncompetitive transplantation as described in panel H (n = 3 independent experiments, symbols represent individual values, bar graphs represent averages, error bars indicate standard deviation [SD], $^{****}P \leq .0001$, 1-way ANOVA, Tukey multiple comparison). (L) Representative FACS plots depicting LSK percentages in the BM of mice of the indicated genotypes after noncompetitive transplantation as described in panel H. (M) LSK percentages in the BM of mice of the respective genotypes as described in panel H (n = 5 independent experiments, symbols represent individual values, bar graphs represent averages, error bars indicate SD, $^{****}P \leq .0001$, 1-way ANOVA, Tukey multiple comparison). (N) Experimental schematic for ex vivo proliferation assay; 50×10^3 LSK cells from mice that received noncompetitive transplantation were sorted and cultured in the continuous presence of mSCF and mTPO for a total of 14 days, after which viable cells were counted using an automated cell-counter. (O) Ex vivo proliferative potential of CRISPR-edited LSKs of indicated genotypes isolated from mice after noncompetitive transplantation (n = 3 independent experiments, bar graphs represent averages, error bars indicate SEM, $^{****}P \leq .0001$, 1-way ANOVA, Tukey multiple comparison). (P) Percentages of $CD45.2^+$ cells in PB of mice that received transplantation with 50 000 CRISPR-edited LSKs of the indicated genotypes together with 0.5×10^6 WBM competitor cells from $CD45.1^+$ mice (n = 7-8 independent experiments, symbols represent averages, error bars indicate SEM, $^{****}P \leq .0001$, 2-way ANOVA, Tukey multiple comparison). FBS, fetal bovine serum; DMOG, dimethyloxalylglycine. DMSO, dimethyl sulfoxide; H_2O_2, hydrogen peroxide; mSCF, mouse stem cell factor; mTPO, mouse thrombopoietin; ns, nonsignificant; NT, nontargeting; ROS, reactive oxygen species.

Figure 2C). Importantly, concomitant *Trp53* loss in *E6l2*-KO Hoxb8 cells abolished p53 activation in the steady state and upon stress (Figure 2B-C) and restored normal cell cycle distribution and apoptotic rates (Figure 2D-E; supplemental Figure 2A-B). Intriguingly, *E6l2-Trp53*-KO Hoxb8 cells not only regained competitive fitness but rapidly outcompeted wild-type cells under all stressors tested in vitro (Figure 2F-G; supplemental Figure 2C).

Next, to investigate the impact of E6l2 loss on the hematopoietic system in vivo, we performed noncompetitive as well as competitive BM transplantation assays using CRISPR/Cas9-engineered HSPCs with *E6l2*-KO, *Trp53*-KO, *E6l2-Trp53*-KO, and nontargeting wild-type genotypes (Figure 2H). We confirmed high CRISPR/Cas9-mediated indel generation in sorted LSKs before transplantation (supplemental Figure 2D). Mice receiving *E6l2*-KO HSPCs in a noncompetitive transplantation setting showed rapidly deteriorating health status in the early posttransplant period and thus had to be euthanized (Figure 2I). Further analysis revealed underlying engraftment failure as morphologically evidenced by severe BM aplasia (Figure 2J-K; supplemental Figure 2E). Mice that received transplants with *E6l2*-KO HSPCs not only showed significantly decreased LSK numbers in vivo (Figure 2L-M) but they also had qualitative defects as demonstrated by reduced ex vivo proliferative potential (Figure 2N-O). After competitive transplantation, *E6l2*-KO cells displayed a severe fitness disadvantage relative to controls as shown by a gradual PB chimerism decrease in the months after transplantation (Figure 2P). In line with our in vitro data, concomitant *Trp53*-KO restored engraftment capacity of *E6l2*-KO HSPCs in both noncompetitive as well as competitive transplantation assays (Figure 2I-K,P), and normalized LSK numbers in the BM and their ex vivo proliferative capacity (Figure 2L-O).

In summary, these results demonstrate that E6l2 deficiency causes an HSPC defect in vitro and in vivo that is rescued by concomitant loss of *Trp53*, thereby promoting clonal outgrowth of double-mutant HSPCs.

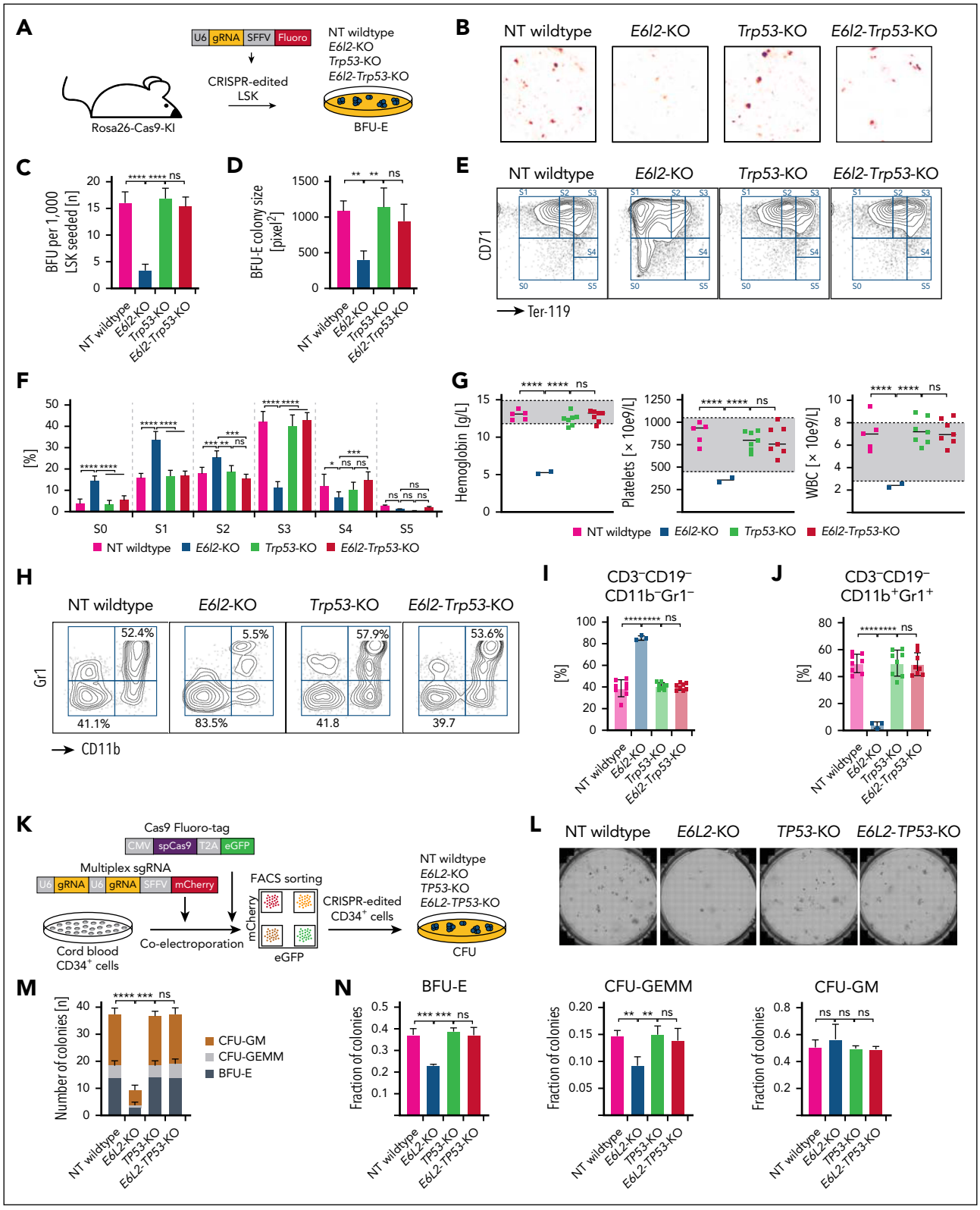

Figure 3. HSPC differentiation blockade due to Ercc6l2 deficiency is overcome upon p53 loss in vitro and in vivo. (A) Experimental schematic for the testing of erythroid differentiation potential in CRISPR-edited LSK cells of the indicated genotypes. (B) Representative images of BFU-E potential of CRISPR-edited cells of respective genotypes. A total of 1.5×10^3 CRISPR-edited LSK cells were sorted and plated in BFU-E selective methylcellulose-based medium and incubated for 10 days. Images were taken via Leica DMI6000B inverted microscope. Analysis was performed using the Colony Area ImageJ plugin resulting in visibly contrasted colonies allowing for automated counting. (C) Automated count of colonies from BFU-E assays as described in panel B (n = 3 independent experiments, bar graphs represent averages, error bars indicate SEM, $^{****}P \leq .0001$, 1-way ANOVA, Tukey multiple comparison). (D) Quantified average colony size from BFU-E assays as described in panel B. Analysis was performed with the Colony Area ImageJ plugin (n = 3 independent experiments, bar graphs represent averages, error bars indicate SEM, $^{**}P \leq .01$, 1-way ANOVA, Tukey multiple comparison). (E) Representative FACS plots demonstrating various stages of erythroid maturation (based on CD71 and Ter-119 expression, stages S0-S5) of cells collected

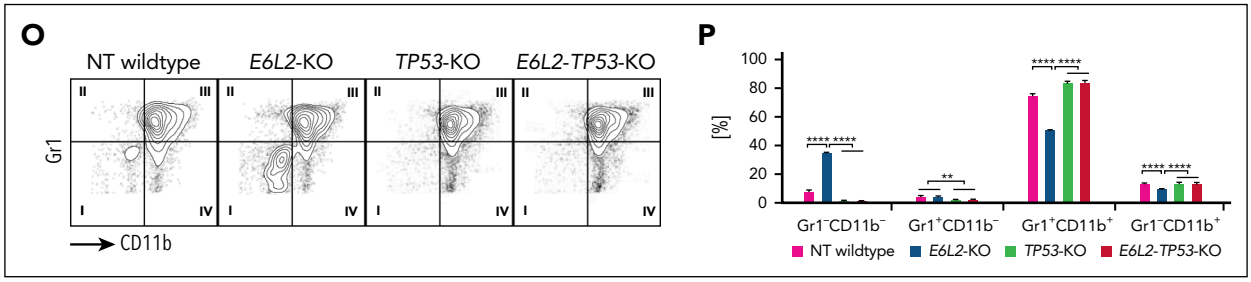

Figure 3 (continued) from BFU-E assays of CRISPR-edited LSK cells of the indicated genotypes as described in panel B. (F) Relative distribution of erythroid maturation stages (S0-S5) from BFU-E assay of CRISPR-edited LSK cells of indicated genotypes as described in panels B and E (n = 3 independent experiments, symbols represent averages, error bars indicate SEM, ****$P \leq .0001$, ***$P \leq .001$, **$P \leq .01$, *$P \leq .05$, 1-way ANOVA, Tukey multiple comparison). (G) PB counts at 2 months of mice that received transplantation with CRISPR-edited LSK cells of indicated genotypes in a noncompetitive manner as described in Figure 2H. Reference ranges are shown in gray-shaded areas. (n = 2-8 independent experiments, symbols represent individual values, horizontal lines represent averages, ****$P \leq .0001$, 1-way ANOVA, Tukey multiple comparison). (H) Representative FACS plots depicting Gr1 and CD11b expression of PB cells 2 months after noncompetitive transplantation of CRISPR-edited LSK cells of respective genotypes. (I) Percentage of $CD11b^{-}Gr1^{-}$ cells in PB of mice 1 month after noncompetitive transplantation of CRISPR-edited LSK cells of indicated genotypes (n = 3-8 independent experiments, symbols represent individual values, bar graphs represent averages, error bars indicate SD, ****$P \leq .0001$, 1-way ANOVA, Tukey multiple comparison). (J) Percentage of $CD11b^{+}Gr1^{+}$ myeloid cells in PB of mice 1 month after noncompetitive transplantation of CRISPR-edited LSK cells of indicated genotypes (n = 3-8 independent experiments, symbols represent individual values, bar graphs represent averages, error bars indicate SD, ****$P \leq .0001$, 1-way ANOVA, Tukey multiple comparison). (K) Experimental schematic for the testing of clonogenic potential in CRISPR-edited $CD34^{+}$ cord blood cells (CB). (L) Representative images of clonogenic potential of CRISPR-edited $CD34^{+}$ CB cells of respective genotypes. A total of 1.0×10^{3} $CD34^{+}GFP^{+}mCherry^{+}$ cells were sorted and plated in cytokine-supplemented methylcellulose-based medium and incubated for 12 days. Images were taken via Leica DMI6000B inverted microscope. (M) Colony counts from CFU assays as described in panel L. Analysis was performed using the Colony Area ImageJ plugin followed by manual counting of the colonies (n = 3 independent experiments, bar graphs represent averages, error bars indicate SD, ****$P \leq .0001$, ***$P \leq .001$ 1-way ANOVA, Tukey multiple comparison). (N) Fraction of BFU-E, CFU-GEMM, and CFU-GM colonies from total colonies of respective genotypes from CFU assays as described in panel L (n = 3 independent experiments, bar graphs represent averages, error bars indicate SD, ***$P \leq .001$, **$P \leq .01$, 1-way ANOVA, Tukey multiple comparison). (O) Representative FACS plots demonstrating erythroid stages 1 through 4 based on immunophenotypic analysis of CD71 and CD235a expression of $CD11b^{-}$ cells collected from CFU assays as described in panel L. (P) Relative distribution of erythroid maturation stages (1-4) from CFU experiments with CRISPR-edited $CD34^{+}$ CBs of indicated genotypes as described in panel L (n = 3 independent experiments, bar graphs represent averages, error bars indicate SEM, ****$P \leq .0001$, **$P \leq .01$, 1-way ANOVA, Tukey multiple comparison). eGFP, enhanced green fluorescent protein; GEMM, granulocyte/erythrocyte/macrophage/megakaryocyte; GM, granulocyte/macrophage; ns, nonsignificant; NT, nontargeting.

Ercc6l2 deficiency causes a myeloid-erythroid maturation blockade that is overcome upon p53 loss in vitro and in vivo

Because patients with ERCC6L2 disease often present with pancytopenia, especially anemia, we next investigated the effects of *E6l2* mutations on terminal hematopoietic differentiation, particularly erythroid maturation. For this, we performed burst-forming unit–erythroid (BFU-E) assays on CRISPR-edited LSK cells of all 4 genotypes (ie, nontargeting wild-type, *E6l2*-KO, *Trp53*-KO, and *E6l2-Trp53*-KO; Figure 3A). E6l2 loss decreased erythroid clonogenic potential with fewer and smaller BFU-E colonies compared with controls (Figure 3B-D; supplemental Figure 3A). Immunophenotypic analyses of these BFU-E colonies[14] revealed an accumulation of $CD71^{-}Ter\text{-}119^{-}$ (S0), $CD71^{+}Ter\text{-}119^{-}$ (S1), $CD71^{+}Ter\text{-}119^{low}$ (S2) immature erythroid progenitor populations with a concomitant decrease in more differentiated $CD71^{+}Ter\text{-}119^{+}$ (S3 and S4) erythroid progenitors in *E6l2*-KO cells (Figure 3E-F). In vivo, mice that received *E6l2*-KO HSPCs in noncompetitive transplantation and that survived the initial posttransplant phase showed BMF with severe, persistent pancytopenia and particularly anemia at 1 month and 2 months after transplant (Figure 3G; supplemental Figure 3B). Moreover, immunophenotypic analysis of the PB of mice engrafted with *E6l2*-KO HSPCs showed a reduced $CD3^{-}CD19^{-}CD11B^{+}Gr\text{-}1^{+}$ population, reflecting typical mature myeloid cells such as granulocytes and macrophages, paralleled by an accumulation of $CD3^{-}CD19^{-}CD11B^{-}Gr\text{-}1^{-}$ cells (Figure 3H-J; supplemental Figure 3C). Notably, the concurrent loss of *Trp53* in *E6l2*-KO HSPCs overcame this maturation defect, normalizing erythroid clonogenic potential in vitro, as well as resolving myeloid-erythroid differentiation with restored PB counts in vivo (Figure 3B-J; supplemental Figure 3A-B).

We next sought to validate our findings in colony-forming unit assays (CFUs) from human $CD34^{+}$ cells. We therefore CRISPR-engineered human cord blood–derived $CD34^{+}$ cells via electroporation of plasmids encoding $RFP657^{+}$ *E6L2*- and/or *TP53*-targeting gRNAs as well as Cas9–enhanced green fluorescent protein expression plasmids. $RFP657^{+}$ enhanced green fluorescent protein–positive cells were sorted 24 hours after electroporation and subsequently plated in cytokine-supplemented CFU media (Figure 3K; supplemental Figure 3D). Indel validation was performed via CRISPR sequencing (supplemental Figure 3E). *E6L2* loss in cord blood $CD34^{+}$ cells strongly impaired overall clonogenic potential, with greater reduction in BFU-E and CFU-GEMM (granulocyte/erythrocyte/macrophage/megakaryocyte) than CFU-GM (granulocyte/macrophage) (Figure 3L-N). Human erythroid colonies showed an erythroid maturation delay as determined by CD71 and CD235 immunophenotyping of $CD11b^{-}$ cells (Figure 3O-P). In line with aforementioned results in mouse HSPCs, *TP53* mutations resolved this maturation block and rescued the clonogenic potential of *E6L2*-KO cells to that of wild-type levels (Figure 3L-P; supplemental Figure 3D-E).

Collectively, these data show that *E6L2* deficiency in HSPCs causes a hematopoietic differentiation defect in vitro and in vivo (most pronounced in the erythroid lineage), which can be resolved by concurrent mutational inactivation of *TP53*.

Combined loss of Ercc6l2 and p53 strongly promotes malignant transformation in vitro

Patients with ERCC6L2 disease and concomitant *TP53*-mutant CH are at high risk for developing myeloid malignancies, in particular AEL.[2] To assess the leukemogenic potential of combined Ercc6l2 and p53 loss, we developed an in vitro

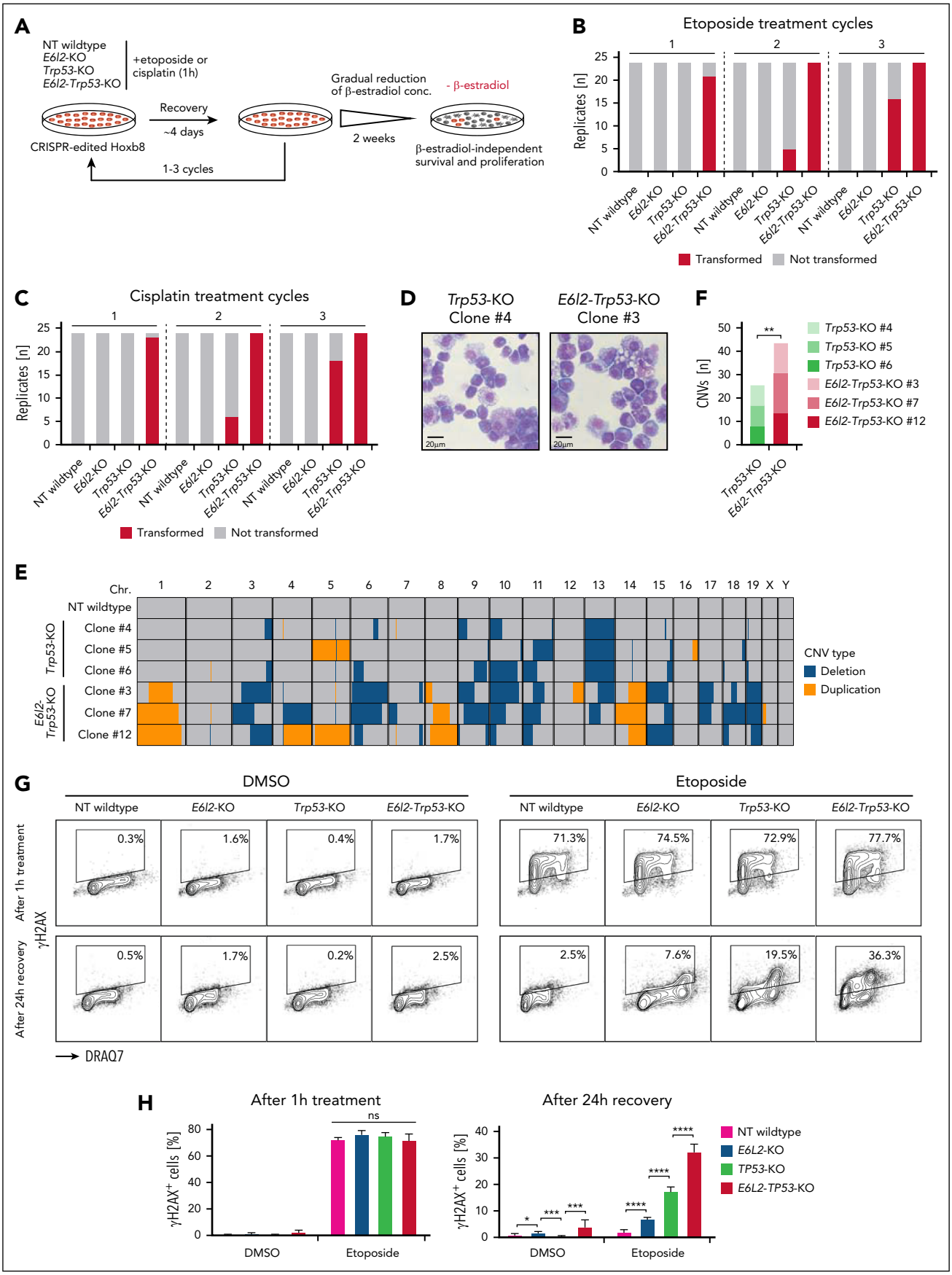

Figure 4.

transformation assay exploiting estrogen-dependent reversible immortalization of Hoxb8 cells. Estrogen withdrawal enabled identification of cells that had acquired genomic alterations substituting for the Hoxb8-driven enhanced self-renewal and differentiation arrest, key features of leukemia. Because none of the genotypes (ie, nontargeting wild type, *E6l2*-KO, *Trp53*-KO, and *E6l2-Trp53*-KO) showed spontaneous estrogen-independent cell growth, cells were treated with DNA-damaging cytotoxic agents followed by gradual estrogen withdrawal (Figure 4A). Although we could not observe any estrogen-independent cell growth in nontargeting wild-type and *E6l2*-KO cells after 3 cycles of etoposide or cisplatin treatment, *Trp53*-KO Hoxb8 cells transformed in 60% to 70% of replicates. Strikingly, combined *E6l2-Trp53* mutations resulted in a greater transformative potential, with 100% of replicates showing estrogen-independent growth, regardless of the DNA-damaging agent used (Figure 4B-C; supplemental Figure 4A). This effect remained evident even when reducing the number of chemotherapeutic cycles to only 1 or 2. Under these experimental conditions, *E6l2-Trp53*-KO cells nonetheless showed nearly 100% transformation rates, whereas *Trp53*-KO cells transformed in only 20% of replicates after 2 chemotherapy cycles, and no transformation was seen after only 1 cycle (Figure 4B-C; supplemental Figure 4B-C). Furthermore, no difference between gRNAs used to introduce *E6l2* mutations were apparent, excluding off-target mutagenic lesions as a cause for the increased malignant transformation observed in *E6l2-Trp53*-KO as compared with *Trp53*-KO Hoxb8 cells (supplemental Figure 4D-F). Transformed cells showed dysplastic- and blast-like cytomorphological features with an immature immunophenotype with no apparent differences between *Trp53*-KO or *E6l2-Trp53*-KO transformed cells (Figure 4D; supplemental Figure 4G-H). Whole-genome sequencing revealed multiple large copy-number alterations (CNAs) reminiscent of the complex karyotypes associated with *TP53*-mutant AML.[15] However, the absolute number of CNAs was significantly higher in transformed *E6l2-Trp53*-KO than *Trp53*-KO cells with a particular numerical increase in duplications (Figure 4E-F; supplemental Figure 5A-F). Furthermore, no recurrent mutations in leukemia-associated genes could be detected (supplemental Table 6). Importantly, nontargeting wild-type Hoxb8 control cells did not carry any detectable CNAs (Figure 4E).

Given the known roles for p53 and E6l2 in DNA damage response, we investigated the impact of single or combined loss of E6l2 and p53 on the accumulation of DNA damage. Using flow cytometric gH2AX measurements after etoposide treatment (Figure 4G-H), we observed high levels of DNA damage 1 hour after chemotherapy treatment irrespective of the genotype. After drug washout and 24-hour recovery, gH2AX staining returned to near baseline levels in nontargeting wild-type Hoxb8 cells. In stark contrast, *E6l2*-KO cells showed persistent DNA damage, which was even further increased in *Trp53*-KO Hoxb8 cells. Of note, *E6l2-Trp53*-KO Hoxb8 cells showed additive levels of persistent DNA damage, thereby providing a plausible explanation for their enhanced transformative potential (Figure 4G-H). This finding could be validated using a DNA-damaging agent with another mode of action (cisplatin; supplemental Figure 5G). Interestingly, we also observed a small genotype-specific difference in DNA damage levels in DMSO-treated cells at baseline (Figure 4G-H). In summary, our data demonstrate that loss of E6l2 causes persistent DNA damage but is insufficient to drive malignant transformation. By contrast, combined loss of E6l2 and p53 results in an increased DNA damage load and strongly promotes malignant transformation to an even higher degree than inactivation of the prototypical tumor suppressor p53 alone.

Concurrent mutational inactivation of Ercc6l2 and p53 in murine HSPCs gives rise to AML with an erythroid phenotype in vivo

To investigate the leukemogenic potential in vivo, we exposed mice to 2 doses of sublethal γ-irradiation 3 and 4 months after noncompetitive as well as competitive transplantation with CRISPR/Cas9-engineered HSPCs of all 4 genotypes (ie, nontargeting wild type, *E6l2*-KO, *Trp53*-KO, and *E6l2-Trp53*-KO). Recipient mice were monitored for survival and the occurrence of malignancies (Figure 5A). Although mice receiving nontargeting wild-type HSPCs showed no signs of sickness, the few mice that had survived the peritransplant period after receiving *E6l2*-KO HSPCs in a noncompetitive manner rapidly succumbed to BMF after irradiation with no signs of malignancy (Figure 5B). Intriguingly, mice that had received *E6l2-Trp53*-KO HSPCs showed a significantly shorter survival than mice receiving *Trp53*-KO HSPCs, both in the noncompetitive as well as competitive transplantation settings (Figure 5B-C). In both groups, primary cause of death was a progressive decline in general health necessitating euthanasia. At time of necropsy, virtually all mice had developed hematologic malignancies. Not only did *E6l2-Trp53*-KO mice develop hematologic malignancies earlier than *Trp53*-KO mice but there was also a striking difference in the type of malignancies (Figure 5D; supplemental Figure 6A). In the noncompetitive transplant format, *Trp53*-KO mice never developed AML but mainly

Figure 4. Malignant transformation in vitro upon combined loss of Ercc6l2 and p53. (A) Experimental schematic of transformation assays using Cas9-Hoxb8 cells. Cas9-Hoxb8 of various genotypes were exposed to etoposide (40mM) or cisplatin (15mM) for 1 hour. Thereafter, drugs were washed out, and cells were allowed to fully recover. Cells were treated for a total of 1 to 3 chemotherapy cycles after which β-estradiol was gradually removed from the supernatant and cells were monitored for β-estradiol–independent cell growth. (B) Rates of transformation of Cas9-Hoxb8 cells of respective genotypes after treatment with etoposide as determined by β-estradiol–independent cell growth after 1 to 3 cycles of etoposide treatment cycles (n = 2 independent experiments). (C) Rates of transformation of Cas9-Hoxb8 cells of respective genotypes after treatment with cisplatin as determined by β-estradiol–independent cell growth after 1 to 3 cycles of cisplatin treatment cycles (n = 2 independent experiments). (D) Representative cytospin images of transformed Cas9-Hoxb8 cells of the indicated genotypes. Scale bars, 20 μm. (E) Detailed CNV analysis via whole-genome sequencing of parental (nontargeting wild type) and transformed Cas9-Hoxb8 cells of indicated genotypes treated with 3 cycles of etoposide. (F) Number of chromosomal CNVs in transformed Cas9-Hoxb8 cells of indicated genotypes treated with 3 cycles of etoposide (n = 3 independent experiments, stacked bar graphs represent total number of CNVs, $^{**}P \leq .01$ Student *t* test). (G) Representative FACS plots of Cas9-Hoxb8 cells showing DNA damage as determined by gH2AX positivity 1 and 24 hours after DMSO or etoposide treatment. (H) Quantification of the percentages of $gH2AX^+$ Cas9-Hoxb8 cells of indicated genotypes 1 or 24 hours after etoposide treatment for 1 hour or treated with DMSO control (bar graphs represent averages, error bars indicate SEM, $^{****}P \leq .0001$, $^{***}P \leq .001$, $^{*}P \leq .05$, 1-way ANOVA, Tukey multiple comparison). Chr, chromosome; CNV, copy number variant; DMSO, dimethyl sulfoxide; ns, nonsignificant; NT, nontargeting.

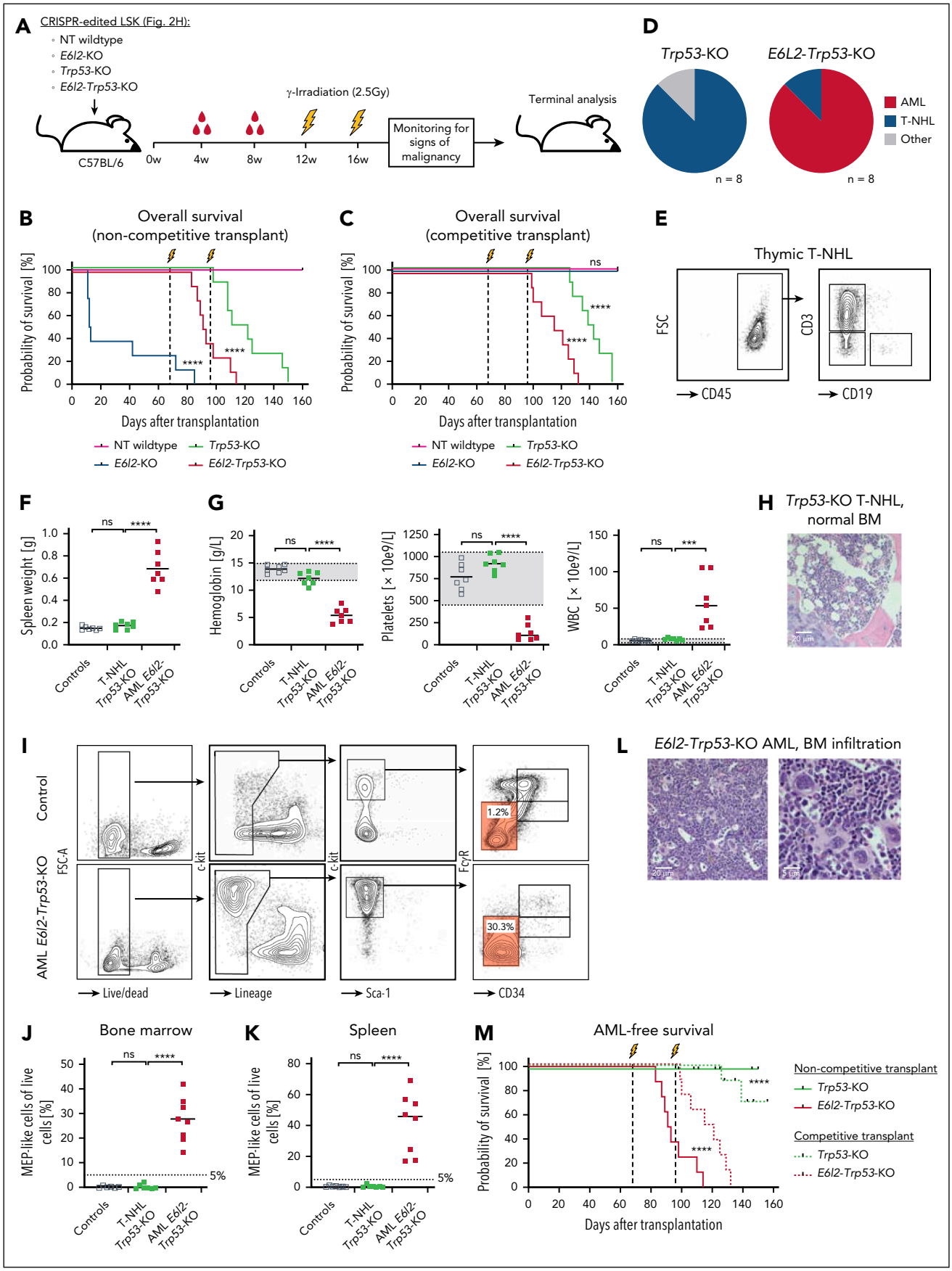

Figure 5.

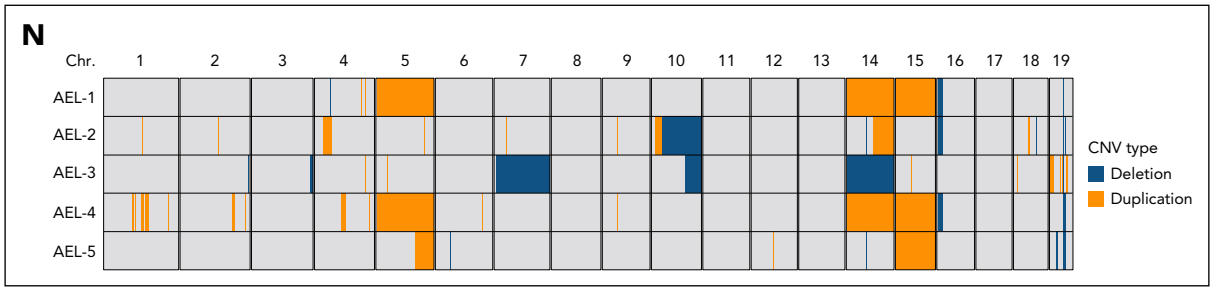

Figure 5. (continued) In vivo development of AML with an erythroid phenotype upon concurrent mutational inactivation of Ercc6l2 and p53. (A) Experimental schematic for the induction of malignant transformation in vivo. Mice were exposed to sublethal irradiation at 3 and 4 months and monitored for signs of malignancy development thereafter. (B) Overall survival analysis of C57BL/6 mice that received noncompetitive transplantation with CRISPR-edited LSK cells of the indicated genotypes. Sublethal irradiation is denoted by vertical dashed lines (animals per group n = 8, $^{****}P \leq .0001$, Mantel-Cox test). (C) Overall survival analysis of C57BL/6 mice that received transplantation with CRISPR-edited LSK cells of the indicated genotypes in a competitive manner (ie, together with CD45.1$^+$ WBM cells as described in Figure 2H). Sublethal irradiation is denoted by vertical dashed lines (animals per group n = 8, $^{****}P \leq .0001$, Mantel-Cox test). (D) Pie chart depicting types of malignancies that developed in mice that received transplantation with CRISPR-edited LSK cells of indicated genotypes in a noncompetitive manner. (E) Representative FACs plots of T-NHLs showing uniformly high expression of CD3. (F) Spleen weight of mice that received noncompetitive transplantation with CRISPR-edited LSK cells of indicated genotypes compared with healthy controls (animals per group n = 7, symbols represent individual values, horizontal lines represent averages, $^{****}P \leq .0001$, 1-way ANOVA, Tukey multiple comparison). (G) Hemoglobin, platelet, and WBC count of mice that received noncompetitive transplantation with CRISPR-edited LSK cells of indicated genotypes compared with healthy controls (animals per group n = 7, symbols represent individual values, horizontal lines represent averages, $^{****}P \leq .0001$, $^{***}P \leq .001$, 1-way ANOVA, Tukey multiple comparison). Reference ranges are shown in gray-shaded areas. (H) Representative H&E-stained BM histology showing normal BM architecture of a mouse that received noncompetitive transplantation with *Trp53*-KO LSK cells in which T-NHL development occurred. Scale bar, 20 μm. (I) Representative FACS plots demonstrating increase in MEP-like blast population in the BM of AML-bearing mice compared with healthy controls. Percentages in red-shaded gates are referring to total live cells. (J) Frequency of MEP-like blasts in the BM of mice that developed AML and T-NHLs compared with healthy control mice (animals per group n = 7-8, symbols represent individual values, horizontal line represents averages, $^{****}P \leq .0001$, 1-way ANOVA, Tukey multiple comparison). (K) Frequency of MEP-like blasts in the spleen of mice that developed AML or T-NHLs compared with healthy control mice (animals per group n = 7-8, symbols represent individual values, horizontal line represents averages, $^{****}P \leq .0001$, 1-way ANOVA, Tukey multiple comparison). (L) Representative H&E-stained BM histology showing infiltration with blast-like cells in a mouse that received noncompetitive transplantation with *E6l2-Trp53*-KO LSKs that developed AML. Scale bar, 20 μm in the left panel and 5 μm in the right panel. (M) AML-free survival of mice that received transplantation both in a noncompetitive as well as competitive manner with CRISPR-edited LSK cells of the indicated genotypes (animals per group n = 8, $^{****}P < .0001$, Mantel-Cox test). (N) Detailed CNV analysis via whole-genome sequencing of 5 different AELs developed in E6l2-Trp53-KO mice. CNV, copy number variant; FcγR, Fc gamma receptor; FSC-A, forward scatter-area; MEP, megakaryocyte-erythroid progenitors; ns, nonsignificant; NT, nontargeting; T-NHL, T-cell non-Hodgkin lymphoma; WBC, white blood cell.

localized T-cell non-Hodgkin lymphomas presenting with a mediastinal mass and no signs of spleen or BM involvement, a well-known phenomenon in p53-mutant mouse models (Figure 5D-H; supplemental Figure 6A-E).[16,17] Intriguingly, almost all mice receiving *E6l2-Trp53*-KO HSPCs developed AML as demonstrated by BM and spleen infiltration with immature, blast-like cells resembling megakaryocyte-erythroid progenitors based on Lin$^-$c-kit$^+$Sca-1$^-$CD34$^-$FcγR$^-$ immunophenotype (Figure 5D,I). We therefore defined AML-bearing mice by the presence of a megakaryocyte-erythroid progenitor–like blast population of >5% in the BM and/or the spleen (Figure 5J-K). Together with massive splenomegaly and severe cytopenias, these findings confirm development of AEL according to the Bethesda criteria,[18] further supported by CD45 negativity and high levels of CD71 (transferrin receptor) expression (Figure 5F-G; supplemental Figure 6F-G). BM histology confirmed the presence of blast-like cells distorting normal BM architecture. These cells were highly reminiscent of immature erythroid progenitors with a round central nucleus, dispersed to finely reticulated chromatin, 1 or several nucleoli, and a deeply basophilic and agranular cytoplasm (Figure 5L; supplemental Figure 6H). These findings were largely mirrored in the competitive transplantations, in which mice engrafted with *E6l2-Trp53*-KO HSPCs developed AELs whereas mice that received transplantation with *Trp53*-KO HSPCs mice predominantly developed T-cell non-Hodgkin lymphomas (supplemental Figure 6A-C). Calculating AML-free survival confirmed the enhanced leukemogenic potential in the setting of combined loss of E6l2 and p53 (Figure 5M). Furthermore, whole-genome sequencing analysis of AML cells confirmed complex karyotype in the absence of other recurrent genetic alterations (Figure 5N; supplemental Figure 7A-E; supplemental Table 7). Collectively, our data demonstrate that loss of p53 in *E6l2*-KO HPSCs is necessary for AML development in vivo, particularly of an erythroid phenotype, thereby recapitulating the striking association between E6L2 disease, somatic *TP53* mutations, and AML progression, particularly acute erythroid leukemia, in patients with ERCC6L2 disease.

Ercc6l2 loss causes RS and decreased *Runx1* and *Gata1* expression, thereby driving the BMF phenotype

To gain insight into the molecular mechanisms underlying the BMF phenotype caused by E6l2 loss we performed transcriptional profiling of nontargeting wild-type, *E6l2*-KO, *Trp53*-KO, and *E6l2-Trp53*-KO CRISPR-engineered primary LSK cells in addition to Hoxb8 cells under steady-state conditions, naturally occurring (ie, high cell density), and genotoxic stress (ie, etoposide treatment; Figure 6A). RNA sequencing analysis of CRISPR-engineered LSK cells revealed distinct transcriptional profiles among the different genotypes, with principal component analysis showing clear separation of genotypes (Figure 6B). In Hoxb8 cells, highest variance separation could be seen between stressed and nonstressed conditions irrespective of their genotypes (supplemental Figure 8B-C). Gene set enrichment analysis of the 50 hallmark gene sets revealed the gene sets "g2m checkpoint" and "e2f targets" to be

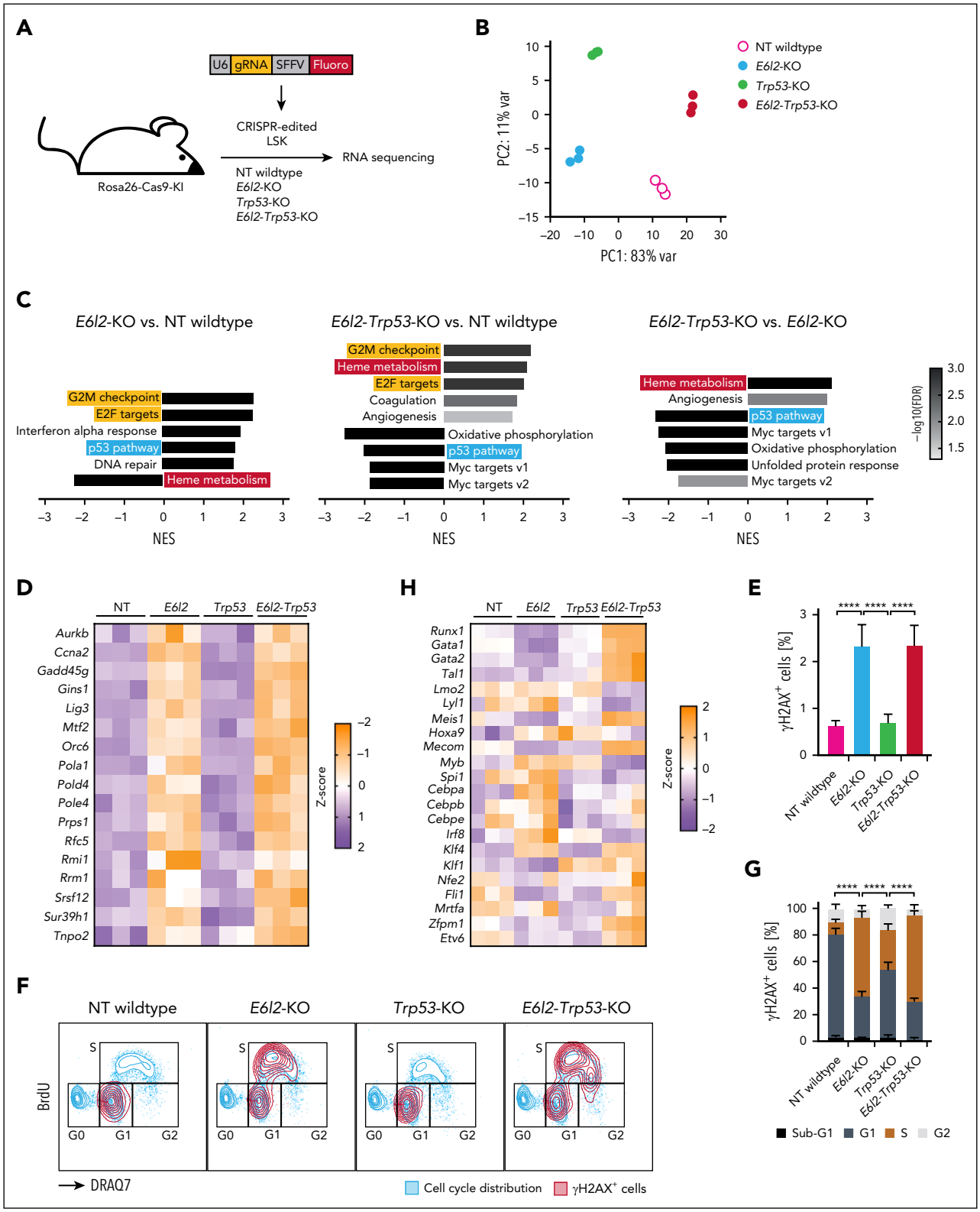

Figure 6. RS and decreased *Runx1* and *Gata1* expression likely cause BMF upon loss of Ercc6l2. (A) Experimental schematic for the transcriptional profiling of CRISPR-engineered LSK cells. BM cells were collected from Rosa26-Cas9-KI mice, subjected to lentiviral-mediated CRISPR editing and subsequently sorted for positively virally integrated cells within LSK$^+$ cells, at which point they were further processed for bulk RNA sequencing. (B) Principal component analysis of CRISPR-engineered LSK cells of respective genotypes demonstrating distinct populations with each 3 technical replicates. (C) Gene set enrichment analysis showing most enriched mouse-ortholog hallmark gene sets in CRISPR-engineered LSK cells of the indicated genotypes. (D) Heat map showing expression of RS signature genes[19] in CRISPR-engineered LSK cells of various genotypes. Row Z scores are normalized. (E) Total gH2AX positivity of Cas9-Hoxb8 cells of indicated genotypes under steady-state conditions (bar graphs represent averages, error bars indicate SEM, ****$P \leq .0001$, 1-way ANOVA, Tukey multiple comparison). (F) Overlay of FACS plots of gH2AX positivity (DNA damage) and bromodeoxyuridine incorporation (cell cycle) in Cas9-Hoxb8 cells under steady-state conditions demonstrating distribution of DNA damage throughout the cell cycle

strongly upregulated in *E6l2*-KO relative to nontargeting wild-type genotypes (Figure 6C; supplemental Figure 8D; supplemental Tables 8-16). Both gene sets, together with additional replication stress (RS)-associated genes, have recently been used to define a RS gene signature.[19] Indeed, this RS gene signature was strongly expressed in *E6l2*-KO and *E6l2-Trp53*-KO CRISPR-engineered LSKs and Hoxb8 cells but not in nontargeting wild-type or *Trp53*-KO genotypes, suggesting induction of RS upon E6l2 loss that is, however, not rescued upon p53 inactivation (Figure 6D; supplemental Figure 8E). Due to the proposed role of E6L2 in DNA replication and mitigation of RS,[9] we set out to validate these findings by linking DNA damage and cell cycle distribution in Hoxb8 cells. Indeed, loss of *E6l2* resulted in increased steady-state DNA damage, as measured by gH2AX, in comparison with nontargeting wild-type Hoxb8 cells, which could be further heightened by high cell density culture conditions or etoposide treatment (Figures 4H and 6E; supplemental Figure 9A). Importantly, although most gH2AX$^+$ cells resided in G1 of the cell cycle in nontargeting wild-type Hoxb8 cells, most gH2AX$^+$ *E6l2*-KO and *E6l2-Trp53*-KO Hoxb8 cells were cycling through S phase (Figure 6F-G; supplemental Figure 9B) demonstrating RS. In line with our data showing p53 activation upon E6l2 loss (Figure 2B), canonical p53 target genes such as *Cdkn1a* were significantly upregulated in *E6l2*-KO CRISPR-engineered LSK and Hoxb8 cells and, as expected, downregulated after concurrent p53 loss (Figure 6C; supplemental Figures 8D and 9C). Altogether, these data reveal that E6l2 deficiency results in RS, which triggers subsequent p53 pathway activation that, in turn, is abrogated due to mutational inactivation of *Trp53*. However, this additional loss of p53 does not rescue RS in E6l2-deficient cells.

Next, we investigated genes downregulated upon loss of *E6l2* with a particular focus on pathways involved in hematopoietic differentiation. Indeed, the hallmark gene set "heme metabolism" was among the most significantly depleted gene sets in *E6l2*-KO CRISPR-engineered LSK and Hoxb8 cells (Figure 6C; supplemental Figure 8D). Similarly, analysis of cell type–specific signature gene sets in Hoxb8 cells revealed enrichment for hematopoietic ageing-associated gene sets (supplemental Figure 9D) and concurrent downregulation of erythroid differentiation genes upon E6l2 loss, which was reversed upon concomitant loss of p53 (supplemental Figure 9D). Moreover, the master regulators of HSPC differentiation as well as of erythroid and megakaryocyte development Runx1 and Gata1[20-23] were significantly downregulated upon loss of E6l2 (Figure 6H). Importantly, expression of *Runx1*, *Gata1*, and the "heme metabolism" gene sets were fully restored in *E6l2-Trp53*-KO cells, even surpassing expression levels seen in nontargeting wild-type Hoxb8 cells (Figure 6H; supplemental Figure 9E-F).

In summary, these results reveal that E6l2 loss not only causes RS leading to p53 pathway activation but also increased expression of hematopoietic ageing-associated genes as well as decreased expression of hematopoietic differentiation genes including *Runx1* and *Gata1*, which likely contributes to the BMF phenotype. Although concomitant loss of p53 restores proper expression of HSPC differentiation genes, it fails to rescue RS, allowing for ongoing DNA damage accumulation.

Discussion

In this study, we developed novel in vitro as well in vivo model systems to gain insights into the thus far poorly understood pathophysiology and molecular mechanisms underlying ERCC6L2 disease, with a special focus on its association with *TP53*-mutant CH and the development of myeloid malignancies.[2]

Our findings suggest a model, in which ERCC6L2 loss in HSPCs results in continuous RS[5,7,8] and sustained, low-level DNA damage, thereby triggering a p53 response. Downstream functional consequences of p53 pathway activation include cell cycle arrest in G1 and increased apoptosis of HSPCs. Moreover, ERCC6L2 deficiency leads to decreased expression of master regulators of hematopoietic differentiation RUNX1 and GATA1 in HSPCs. Together, this causes the BMF disease phenotype characterized by a numerical loss of HSPCs, BM hypocellularity, reduced myeloid-erythroid differentiation potential, and pancytopenia (Figure 7, left panel).

Sporadically acquired somatic *TP53* loss-of-function mutations in ERCC6L2-deficient HSPCs confer a competitive fitness advantage by abrogating the p53 response, overcoming G1 arrest, and reducing apoptosis, leading to clonal expansion over ERCC6L2-deficient HSPCs with wild-type *TP53*. Furthermore, loss of p53 restores expression of RUNX1 and GATA1 in ERCC6L2-deficient HSPCs. Together, this alleviates the BMF disease phenotype (Figure 7, right panel).

Activation of a p53 response has been implicated in the pathogenesis of several other inherited BMF syndromes including Fanconi anemia,[24] Diamond-Blackfan anemia,[25,26] dyskeratosis congenita,[27,28] and Shwachman-Diamond syndrome.[29] Moreover, p53 pathway inactivation by somatic chromosome 1q/*MDM4* trisomy in Fanconi anemia[30] or *TP53* mutations in Shwachman-Diamond syndrome[29] has been shown to improve hematopoietic output. Accordingly, the role of p53 in ERCC6L2 disease is a prime example of an inadequate clonal compensatory mechanism: persistent RS activates p53, which restricts leukemic evolution by preventing excessive DNA damage but simultaneously drives the BMF phenotype in ERCC6L2 disease. Loss of p53 alleviates this hematopoietic defect; however, the inability to resolve RS under these conditions promotes the accrual of DNA damage and markedly heightens leukemic risk (Figure 7).

We have, to the best of our knowledge, generated the first in vitro and in vivo models that faithfully recapitulate all key clinical aspects of ERCC6L2 disease, including somatic gene rescue by p53 inactivation and subsequent leukemic progression. However, several open questions remain. Runx1 and

Figure 6 (continued) stages. (G) Distribution of gH2AX positivity within the cell cycle stages of Cas9-Hoxb8 cells at rest (bar graphs represent averages, error bars indicate SEM, ****$P \leq .0001$, 1-way ANOVA, Tukey multiple comparison). (H) Heat map showing expression of genes implicated as master regulators of hematopoiesis from bulk RNA sequencing obtained from CRISPR-engineered LSK cells. Row Z scores are normalized. BrdU, bromodeoxyuridine; FDR, false discovery rate; NES, normalized enrichment score; NT, nontargeting; var, variance.

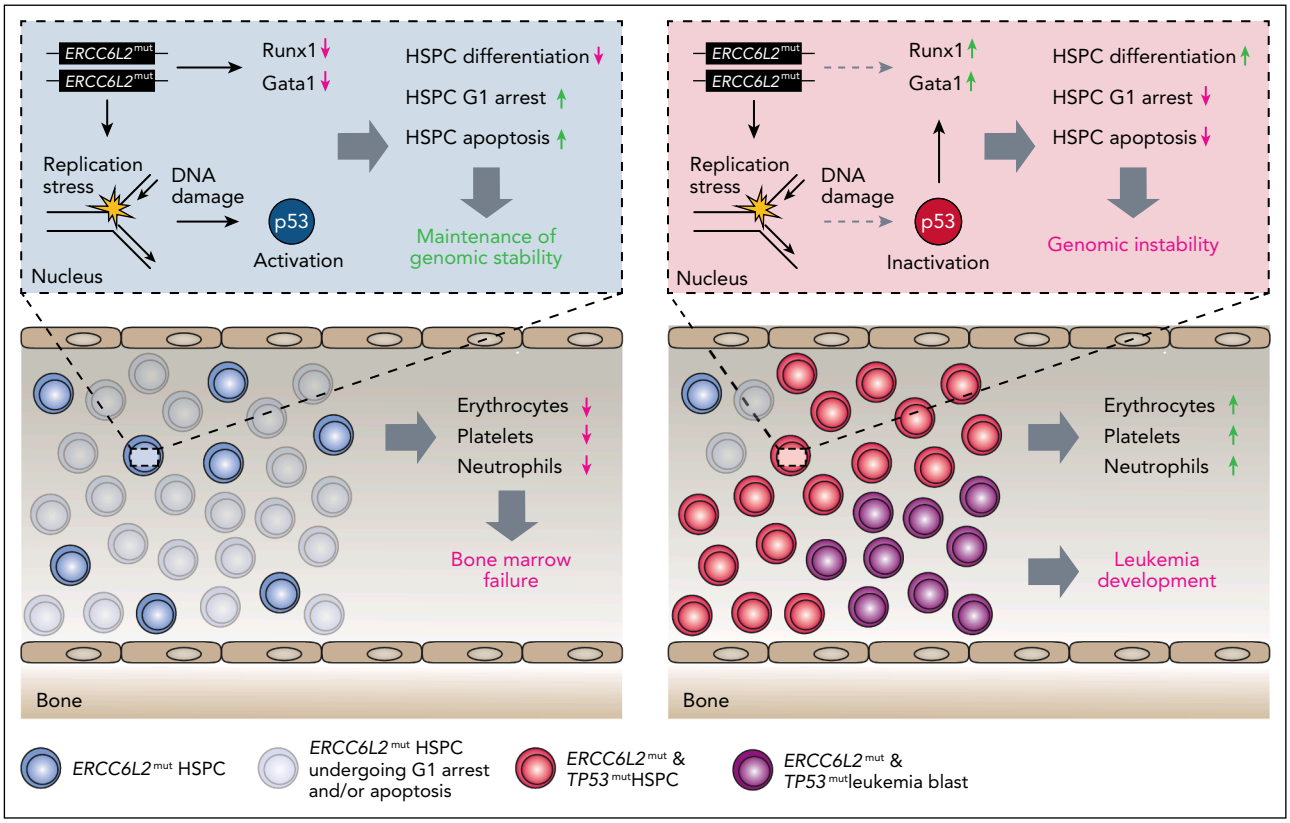

Figure 7. Proposed model for the mechanism underlying the BMF phenotype, clonal compensation via loss of p53, and enhanced leukemogenesis in ERCC6L2 disease. Loss of ERCC6L2 in HSPCs leads to persistent RS and sustained, low-level DNA damage, which activates a p53-dependent stress response. Altogether, this results in G1 cell cycle arrest and increased apoptosis, as well as downregulation of key hematopoietic transcription factors RUNX1 and GATA1, collectively impairing differentiation and leading to BMF, characterized by HSPC depletion and pancytopenia (left panel). Sporadic acquisition of somatic *TP53* loss-of-function mutations in ERCC6L2-deficient HSPCs abrogates the p53 checkpoint, thereby overcoming G1 arrest and apoptosis leading to clonal expansion of *TP53*-mutant HSPCs. Moreover, RUNX1 and GATA1 expression are restored in ERCC6L2-deficient HSPCs upon p53 inactivation. This compensatory mechanism alleviates BMF but not RS resulting in the accumulation of DNA damage and an increased risk of leukemic transformation (right panel). This model highlights the dual role of wild-type p53 activity as both a driver of BMF and a guardian against leukemic progression in the context of ERCC6L2 deficiency.

Gata1 are pivotal transcription factors for normal hematopoiesis,[20-23] and their reduced expression upon loss of ERCC6L2 likely contributes to the BMF phenotype. P53 inactivation restores Runx1 and Gata1 expression. However, because both Runx1 and Gata1 interact with p53 in an antagonistic manner,[31,32] it remains to be elucidated whether E6l2 loss directly results in decreased Runx1 and/or Gata1 expression, or whether this is a consequence of p53 signaling.

Moreover, because loss of E6l2 in Lhx2 cells caused severe BMF phenotype that precluded further mechanistic studies, we had to use Hoxb8 cells, which required additional stressors to elicit the BMF phenotype. Similarly, in vivo ERCC6L2 disease modeling using transplantation-based assays is a good approximation of the clinical scenario but also induces hematopoietic stress. Therefore, future studies using novel transgenic mouse models are warranted to study ERCC6L2 disease under conditions of unperturbed hematopoiesis. This may be particularly relevant because it is unknown why ERCC6L2, despite being ubiquitously expressed, specifically causes a hematopoietic defect. Furthermore, why does ERCC6L2 disease become clinically apparent only relatively late in childhood and in early adolescence but not in infants in whom massive expansion of the hematopoietic system occurs during the first year of life? It is tempting to speculate that a yet-to-be-identified naturally occurring stressor promotes the clinical appearance of BMF in ERCC6L2 disease. Furthermore, it is unclear why ERCC6L2 loss selectively favors *TP53* mutations rather than other forms of p53 inactivation, such as *MDM4* amplifications as seen in Fanconi anemia. Future studies are needed to address these questions.

Acknowledgments

The authors thank the Functional Genomics Center Zurich and the Laboratory Animal Services Center for their support, Angelina Oestmann for assistance with mouse colony management, Susanne Dettwiler for preparation of histology slides, and Tobias Benoit and Robin Kosche for assistance with microscopy.

This work was supported by research grants from the KRAK Physician Scientist Fellowship and the Jacques and Gloria Gossweiler Foundation (R.R.S.); the Sigrid Juselius Foundation, Research Council of Finland, and Finnish Medical Foundation (M.M.); the Swiss National Science Foundation (320030_219676/1; M.G.M.); and the Swiss National Science Foundation (310030_197562/1) and the Helmut Horten Foundation (S.B.).

Authorship

Contribution: R.R.S. designed, performed, and analyzed experiments, and wrote the manuscript; N.K., J.F., E.T., M.T., C.D., D.D.-S., M.L., F.C., C.K., and M.B. helped perform experiments; K.A.Z. helped analyze experiments; N.D., R.S., M.M., K.J.K., M.G.M., and M.L. designed experiments and discussed data; and S.B. directed the study, designed experiments, and wrote the manuscript.

Conflict-of-interest disclosure: The authors declare no competing financial interests.

ORCID profiles: R.R.S., 0000-0003-0846-8508; E.T., 0000-0003-1459-4893; M.T., 0009-0007-2976-0889; C.D., 0000-0002-0843-866X; D.D.-S., 0009-0009-8691-5108; F.C., 0000-0003-4096-4448; C.K., 0009-0000-0681-4265; R.S., 0009-0005-0294-8748; M.M., 0000-0002-8194-7356; K.J.K., 0000-0001-8286-2429; M.G.M., 0000-0002-4676-7931; S.B., 0000-0001-9937-0957.

Correspondence: Steffen Boettcher, Comprehensive Cancer Center Zurich, University of Zurich, and University Hospital of Zurich, Department of Medical Oncology and Hematology, Raemistrasse 100, CH-8091 Zurich, Switzerland; email: steffen.boettcher@usz.ch.

Footnotes

Submitted 6 June 2025; accepted 9 December 2025; prepublished online on *Blood* First Edition 5 January 2026. https://doi.org/10.1182/blood.2025030230.

Presented in abstract form at the 66th annual meeting of the American Society of Hematology, San Diego, CA, 7 to 10 December 2024.

Bulk RNA sequencing and whole-genome sequencing data have been deposited in the Gene Expression Omnibus database and Sequence Read Archive (accession numbers GSE298958 and PRJNA1272635, respectively).

Original data are available from the corresponding author, Steffen Boettcher (steffen.boettcher@usz.ch), on request.

The online version of this article contains a data supplement.

There is a *Blood* Commentary on this article in this issue.

The publication costs of this article were defrayed in part by page charge payment. Therefore, and solely to indicate this fact, this article is hereby marked "advertisement" in accordance with 18 USC section 1734.

REFERENCES

1. Tummala H, Kirwan M, Walne AJ, et al. ERCC6L2 mutations link a distinct bone-marrow-failure syndrome to DNA repair and mitochondrial function. *Am J Hum Genet*. 2014;94(2):246-256.
2. Hakkarainen M, Kaaja I, Douglas SPM, et al. The clinical picture of ERCC6L2 disease: from bone marrow failure to acute leukemia. *Blood*. 2023;141(23):2853-2866.
3. Bluteau O, Sebert M, Leblanc T, et al. A landscape of germ line mutations in a cohort of inherited bone marrow failure patients. *Blood*. 2018;131(7):717-732.
4. Järviaho T, Halt K, Hirvikoski P, Moilanen J, Möttönen M, Niinimäki R. Bone marrow failure syndrome caused by homozygous frameshift mutation in the ERCC6L2 gene. *Clin Genet*. 2018;93(2):392-395.
5. Tummala H, Dokal AD, Walne A, et al. Genome instability is a consequence of transcription deficiency in patients with bone marrow failure harboring biallelic ERCC6L2 variants. *Proc Natl Acad Sci*. 2018;115(30):7777-7782.
6. Douglas SPM, Siipola P, Kovanen PE, et al. ERCC6L2 defines a novel entity within inherited acute myeloid leukemia. *Blood*. 2019;133(25):2724-2728.
7. Zhang S, Pondarre C, Pennarun G, et al. A nonsense mutation in the DNA repair factor Hebo causes mild bone marrow failure and microcephaly. *J Exp Med*. 2016;213(6):1011-1028.
8. Armes H, Bewicke-Copley F, Rio-Machin A, et al. Germline ERCC excision repair 6 like 2 (ERCC6L2) mutations lead to impaired erythropoiesis and reshaping of the bone marrow microenvironment. *Br J Haematol*. 2022;199(5):754-764.
9. Carnie CJ, Armstrong L, Sebesta M, et al. ERCC6L2 mitigates replication stress and promotes centromere stability. *Cell Rep*. 2023;42(4):112329.
10. Platt RJ, Chen S, Zhou Y, et al. CRISPR-cas9 knockin mice for genome editing and cancer modeling. *Cell*. 2014;159(2):440-455.
11. Boettcher S, Miller PG, Sharma R, et al. A dominant-negative effect drives selection of TP53 missense mutations in myeloid malignancies. *Science*. 2019;365(6453):599-604.
12. Doma E, Mayer IM, Brandstoetter T, et al. A robust approach for the generation of functional hematopoietic progenitor cell lines to model leukemic transformation. *Blood Adv*. 2021;5(1):39-53.
13. Wang GG, Calvo KR, Pasillas MP, Sykes DB, Häcker H, Kamps MP. Quantitative production of macrophages or neutrophils ex vivo using conditional Hoxb8. *Nat Methods*. 2006;3(4):287-293.
14. Koulnis M, Pop R, Porpiglia E, Shearstone JR, Hidalgo D, Socolovsky M. Identification and analysis of mouse erythroid progenitors using the CD71/TER119 flow-cytometric assay. *J Vis Exp*. 2011;(54):2809.
15. Rücker FG, Schlenk RF, Bullinger L, et al. TP53 alterations in acute myeloid leukemia with complex karyotype correlate with specific copy number alterations, monosomal karyotype, and dismal outcome. *Blood*. 2012;119(9):2114-2121.
16. Lang GA, Iwakuma T, Suh YA, et al. Gain of function of a p53 hot spot mutation in a mouse model of Li-Fraumeni syndrome. *Cell*. 2004;119(6):861-872.
17. Olive KP, Tuveson DA, Ruhe ZC, et al. Mutant p53 gain of function in two mouse models of Li-Fraumeni syndrome. *Cell*. 2004;119(6):847-860.
18. Kogan SC, Ward JM, Anver MR, et al. Bethesda proposals for classification of nonlymphoid hematopoietic neoplasms in mice. *Blood*. 2002;100(1):238-245.
19. Takahashi N, Kim S, Schultz CW, et al. Replication stress defines distinct molecular subtypes across cancers. *Cancer Res Commun*. 2022;2(6):503-517.
20. Shivdasani RA, Fujiwara Y, McDevitt MA, Orkin SH. A lineage-selective knockout establishes the critical role of transcription factor GATA-1 in megakaryocyte growth and platelet development. *EMBO J*. 1997;16(13):3965-3973.
21. Okuda T, van Deursen J, Hiebert SW, Grosveld G, Downing JR, Downing JR. AML1, the target of multiple chromosomal translocations in human leukemia, is essential for normal fetal liver hematopoiesis. *Cell*. 1996;84(2):321-330.
22. Fujiwara Y, Browne CP, Cunniff K, Goff SC, Orkin SH. Arrested development of embryonic red cell precursors in mouse embryos lacking transcription factor GATA-1. *Proc Natl Acad Sci*. 1996;93(22):12355-12358.
23. Wang Q, Stacy T, Binder M, Marin-Padilla M, Sharpe AH, Speck NA. Disruption of the Cbfa2 gene causes necrosis and hemorrhaging in the central nervous system and blocks definitive hematopoiesis. *Proc Natl Acad Sci*. 1996;93(8):3444-3449.
24. Ceccaldi R, Parmar K, Mouly E, et al. Bone marrow failure in fanconi anemia is triggered by an exacerbated p53/p21 DNA damage response that impairs hematopoietic stem and progenitor cells. *Cell Stem Cell*. 2012;11(1):36-49.
25. Narla A, Ebert BL. Ribosomopathies: human disorders of ribosome dysfunction. *Blood*. 2010;115(16):3196-3205.
26. Zhang Y, Lu H. Signaling to p53: ribosomal proteins find their way. *Cancer Cell*. 2009;16(5):369-377.
27. Bellodi C, Kopmar N, Ruggero D. Deregulation of oncogene-induced senescence and p53 translational control in X-linked dyskeratosis congenita. *EMBO J*. 2010;29(11):1865-1876.
28. Chin L, Artandi SE, Shen Q, et al. p53 deficiency rescues the adverse effects of

telomere loss and cooperates with telomere dysfunction to accelerate carcinogenesis. *Cell*. 1999;97(4):527-538.

29. Kennedy AL, Myers KC, Bowman J, et al. Distinct genetic pathways define pre-malignant versus compensatory clonal hematopoiesis in Shwachman-Diamond syndrome. *Nat Commun*. 2021;12:1334.

30. Sebert M, Gachet S, Leblanc T, et al. Clonal hematopoiesis driven by chromosome 1q/MDM4 trisomy defines a canonical route toward leukemia in Fanconi anemia. *Cell Stem Cell*. 2023;30(2):153.e9-170.e9.

31. Trainor CD, Mas C, Archambault P, Di Lello P, Omichinski JG. GATA-1 associates with and inhibits p53. *Blood*. 2009;114(1):165-173.

32. Morita K, Suzuki K, Maeda S, et al. Genetic regulation of the RUNX transcription factor family has antitumor effects. *J Clin Invest*. 2017;127(7):2815-2828.